iScience

Article

# Pathways to high-performance extreme ultra-violet lithography resists: Dissociative electron attachment to pentafluoro-phenyl triflate

## Graphical abstract

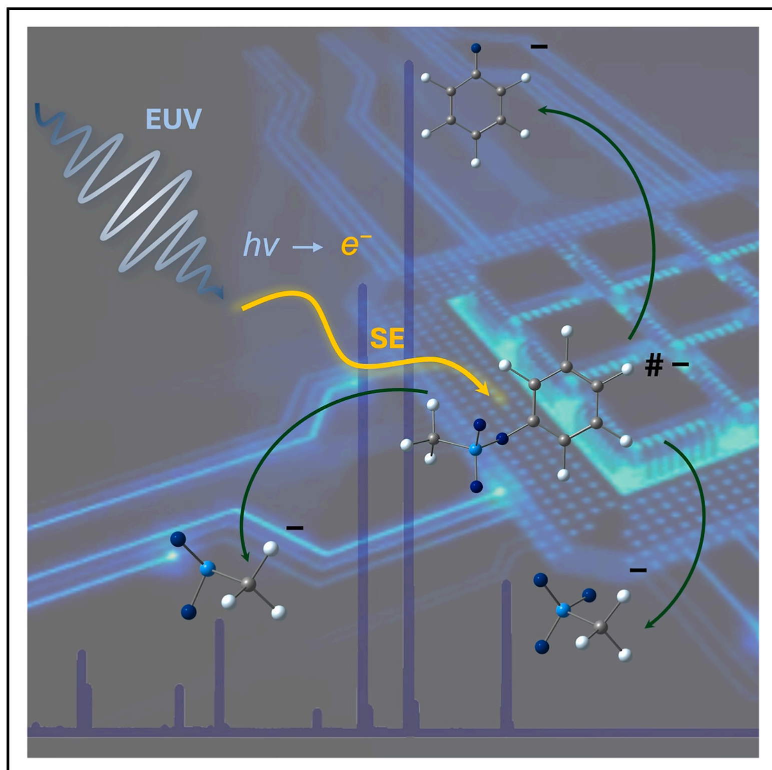


## Highlights

- DEA quenches acid formation in asymmetric neutral ester PAGs for EUVL
- Potential paths to sensitization of EUVL resist materials
- Molecular design for electron induced acid generation in EUVL resist chemistry
- Symmetric neutral ester PAGs for DEA-driven EUVL resist chemistry


## Authors

Mónica Mendes, Reza Tafrishi, Pedro Guerra, Fabian Holzmeier, Oddur Ingólfsson, Filipe Ferreira da Silva

## Correspondence

odduring@hi.is (O.I.),
f.ferreiradasilva@fct.unl.pt (F.F.d.S.)


## In brief

Analytical chemistry; Analytical chemistry analysis; Theoretical organic chemistry; Chemical compound

Mendes et al., 2025, iScience *28*, 114020
December 19, 2025 © 2025 The Authors. Published by Elsevier Inc.
https://doi.org/10.1016/j.isci.2025.114020

CellPress

iScience

CellPress
OPEN ACCESS

Article

# Pathways to high-performance extreme ultra-violet lithography resists: Dissociative electron attachment to pentafluoro-phenyl triflate

Mónica Mendes,[1,4] Reza Tafrishi,[2,4] Pedro Guerra,[1] Fabian Holzmeier,[3] Oddur Ingólfsson,[2,5,*] and Filipe Ferreira da Silva[1,*]
[1]CEFITEC, Department of Physics, NOVA University Lisbon, School of Science and Technology, 2829-516 Caparica, Portugal
[2]Department of Chemistry, Univercity of Iceland, Science Institute, Dunhagi 3, 107 Reykjavík, Iceland
[3]IMEC, Kapeldreef 75, 3001 Leuven, Belgium
[4]These authors contributed equally
[5]Lead contact
*Correspondence: odduring@hi.is (O.I.), f.ferreiradasilva@fct.unl.pt (F.F.d.S.)
https://doi.org/10.1016/j.isci.2025.114020

## SUMMARY

To fully enfold the significant advantage of extreme ultraviolet lithography (EUVL) in the high-volume realization of the next generation technology nodes, high sensitivity EUVL resist formulations, tailored to the electron driven chemistry triggered in EUVL are essential. Here we address this by studying low energy electron-driven chemistry of pentafluorophenyl triflate, a neutral phenyl ester photo acid generator (PAG), i.e., a critical component of the commonly used chemically amplified resist (CAR) formulations. We present an experimental and theoretical study on dissociative electron attachment (DEA) to this compound, and we show that DEA rather quenches, than promotes its intended acid generation. We argue that these findings are general to currently proposed neutral ester PAGs for EUVL, and we propose an approach where this may be upturned, and DEA may contribute significantly to the critical acid generation in CARs up on EUV exposure and thus the sensitivity of these resists.

## INTRODUCTION

Recently extreme ultraviolet lithography (EUVL) has been introduced into the high-volume manufacturing of the latest generation of computer chips, complementary to the conventional deep ultraviolet lithography (DUVL).[1] This constitutes a transition from the typical use of 248 or 193 nm (5.0 and 6.4 eV, respectively) to 13.5 nm (92 eV) light, to induce the chemistry in the respective resist materials, that in turn enables the required patterning. Generating and handling light of this short wavelength is technically very challenging,[1,2] but due to the direct proportionality of the printing resolution to the wavelength (resolution $\propto$ wavelength/numerical aperture), the potential gain in resolution and thus in the transistor density is significant.[3] This is critical in realization of new and improved chip design, specifically the complementary field-effect transistors, introduction of which would be a significant step toward the much-needed lower energy consumption in computer processing.[4] However, while the chemical conversion of the resist material in DUVL is driven by light (photochemistry), 13.5 nm is ionizing radiation and the chemistry induced within the respective resist materials is expected to be at large electron driven.[5–7] The photon energy at 13.5 nm is 92 eV and primary photoelectrons generated in the resist material through valence ionization are thus in the energy range of about 85–65 eV, depending on the ionization energy of the respective resist materials. These electrons, in turn, cause further secondary and tertiary ionization events, which along with other inelastic scattering processes lead to a dynamic secondary electron energy distribution within the resist material that is non-negligible at the verge of the 0 eV threshold.[5,6,8,9] In this energy range electron-induced molecular fragmentation and rearrangement reactions may take place through dissociative electron attachment (DEA), dissociative ionization (DI), dipolar dissociation (DD), and neutral dissociation (ND).[10] From these, DI is a non-resonant process with an onset at the respective thresholds and a maximum at around 50–100 eV, after which it gradually tails off as the energy transfer gets less efficient. DEA, on the other hand, is a resonant process proceeding in narrow energy ranges below the ionization energy of the respective processes and is by far the most efficient in a narrow energy range (few meV) close to the 0 eV threshold. While the former leads to the formation of a positively charged ion and neutral fragment(s) the latter leads to the formation of a thermodynamically stable anionic fragment and neutral fragment(s). ND and DD are like DI, non-resonant processes, and are both relaxation processes proceeding from electronically excited states with an onset at the respective thresholds. Here the former leads to neutral fragments while the latter leads to the formation of the respective ion pair. Except for the thermochemically stable ions formed in these processes, the fragments formed are

This is an open access article under the CC BY-NC-ND license (http://creativecommons.org/licenses/by-nc-nd/4.0/).

mostly radical, reactive species, and likely to play an important role in the EUV-induced resist chemistry.

The photo and secondary electron energy distribution is dynamic and material dependent, and the chemical response, i.e., the ND, DI, and DEA contributions and their branching ratios, are also material dependent and depend on the electron energy distribution. This makes the chemistry behind the solubility switching in EUVL significantly more complex than the photochemistry driving the patterning in DUVL, however, if well understood it also offers the opportunity of enhancing the sensitivity to EUVL exposure and directing the resulting chemistry. All these processes may be active and contribute to the solubility switching, as has been shown in several studies,[11–16] and specifically for DEA for the reactivity of tin-based molecular resists.[16] This may open opportunities as DEA, due to its resonant nature and bond selectivity, is arguably easiest to manipulate through rational molecular design to increase cross sections and direct bond ruptures (see Ingólfsson, 2019[10] and references therein).

In the last decade significant effort has been directed toward the evaluation of existing resist materials and their modifications, as well as development of new materials and concepts to provide suitable EUVL resist formulations. Specifically, it is desirable to enhance the sensitivity of the resist material and achieve the desired resolution without compromising linewidth roughness and line edge roughness (LER) of the printed patterns.[17] In this context the introduction of metallic and non-metallic sensitizers has been investigated, with chemically amplified resists (CARs),[18–21] polymeric non-CARs,[22,23] and hybrid resist materials.[24–26] Much attention has also been given to inorganic, metal oxide based photoresists containing Sn, Zr, Zn, or Hf[27–34], and rare-earth ion doped and heterometallic tin oxo-clusters have been studied.[35,36] More exotic materials such as metal-organic frame works,[37,38] polypeptides,[38] sugars,[39] and fullerene-containing polymers[40] have also been explored. Furthermore, for increased photon absorption and thus increased sensitivity, direct fluorination of polymeric resist materials, photo acid generators (PAGs) in CARs, and of the ligand structure in metallic oxo-clusters has been probed in a number of studies.[41–46] In CARs, the PAG plays a determining role by dissociation and generation of a strong acid upon exposure. The so-formed acid catalyzes the desired reactions within the resist material, which, in turn, changes its solubility in the exposed area. In EUVL, the quantum yield is considerably lower than in DUVL, due to lower absorbance, while the number of available photons in an EUV scanner has also decreased significantly compared to the DUV technology. Sensitivity enhancement has therefore been one of the main goals in the development of new resist formulations. A number of approaches have been taken in this direction, including higher PAG loads or the application of higher EUV absorbant PAGs as potential pathways for the design of high-performance CARs for EUVL.[47–49] Currently, ionic PAGs are the most common, but neutral PAGs like oxime sulfonates, aryl sulfonates, and polymeric PAGs[50–52] are also being explored as they allow a higher PAG concentration in the photoresist material without phase separation due to the polarity differences between polymers and ionic PAGs,[53–55] and may thus lower the EUV dose needed for the respective solubility switching.[49] Furthermore, as the absorption cross-section of fluorine at 13.5 nm is more than five times that of carbon and 130 times higher than that of hydrogen; higher degree of fluorination of the respective PAGs may be a way to further decrease the required load.[41,51,56] To move forward in the development of high performance EUVL resist materials it is important to understand the chemistry induced upon exposure and eventually use that understanding to design higher sensitivity and better performing EUVL resist materials.

In this context, aryl and allyl trifluoromethanesulfonates (triflates) have been studied as potential pathways for neutral PAGs for generation of the strong trifluoromethanesulfonic acid (triflic acid). In crossed beam and flowing afterglow Langmuir probe studies, it was shown that DEA at low incident electron energies leads predominantly to formation of the triflic anion from its acid and allyl esters.[57,58] In photoionization of phenyl triflate at 92 eV photon energy,[59] on the other hand, the main fragmentation channels were associated with sequential $SO_2$, $CF_3$, CO, and $C_2H_2$ loss, and potential precursors for the triflic acid were not observed. Consistent with these observations, EUV exposures of an epoxy-based cross-linking photoresist with perfluorinated phenyl triflate as a PAG showed no enhancement of the degree of polymerization.[47]

Perfluorination of phenyl triflate, however, is expected to enhance its electron attachment cross section and thus have the same effect for DEA and may also alter the fragmentation efficiency and the branching ratios upon photo and/or electron ionization.

In context to the potential of this pathway, and perfluorinated phenyl triflate as PAG in CARs for EUVL, we have undertaken a comprehensive study on the fragmentation of this compound upon electron attachment (DEA). In the current contribution, we present experimental and theoretical data on the fragmentation of pentafluorophenyl triflate upon electron attachment. The fragmentation pathways are discussed in context to the underlying resonances and the calculated thermochemical thresholds for the respective processes. The findings are clear and general in context to the potential of neutral ester PAGs in EUVL CARs and provide guidelines for possible molecular modifications that may be expected to improve the performance of this group of PAGs in EUVL.

## RESULTS

### Negative ion formation from pentafluorophenyl triflate

Figure 1 shows a cumulative negative ion mass spectrum of pentafluorophenyl triflate. The spectrum is the sum of mass spectra recorded with 10 meV intervals in the energy range from 0 to 10 eV and covers the m/z range from 25 to 330. For clarity the linear formula of the fragments and the respective m/z ratio is shown at the individual peaks, and the molecular structure of pentafluorophenyl triflate optimized at the B3LYP/def2-TZVP level of theory is shown as an inset.

The most significant contributions are observed at m/z 183, 149, and 133. From these, we attribute the m/z ratios 183 and 133 to the complementary ions $C_6F_5O^-$ and $CF_3SO_2^-$, formed through rupture of the S–OC bond of the sulfonic ester, with charge retention on the aromatic moiety and the sulfonyl rest, respectively. The m/z ratio 149, on the other hand, is attributed

CellPress
OPEN ACCESS

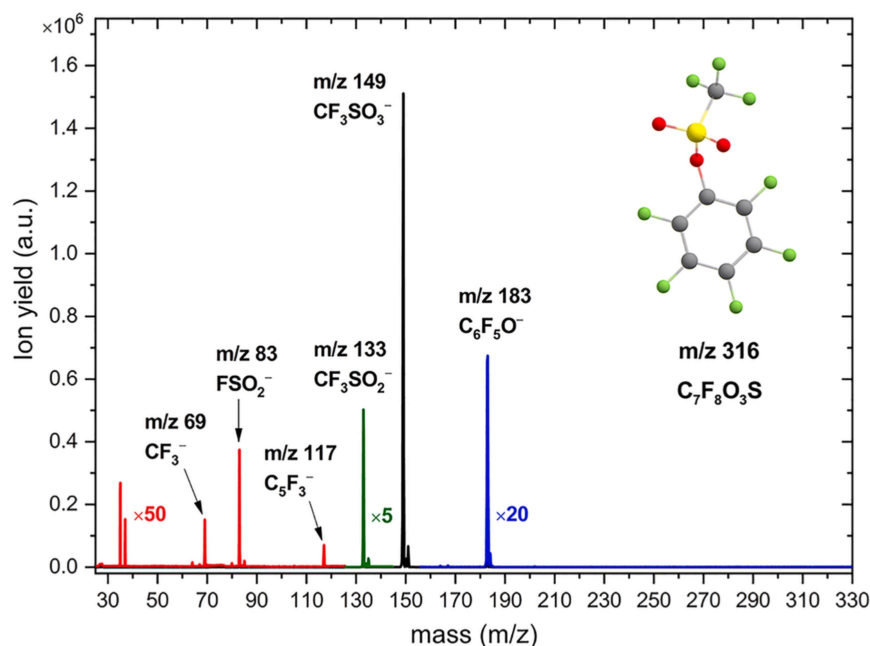


**Figure 1. Cumulative negative ion mass spectrum of pentafluorophenyl triflate**

The m/z ranges 25–125, 125–140 and 155–330 are amplified ×50, ×5, and ×20, respectively. The peaks at m/z 35 and 37 are the $Cl^-$ isotopes from residues of the $CCl_4$ calibration gas.

to rupture of the SO–C sulfonic ester bond with charge retention on the trifluoromethanesulfonate, i.e., formation of the triflate anion $CF_3SO_3^-$. Further fragments are observed at the m/z ratios 117, 83, and 69, though with orders of magnitude lower intensities. In accordance with the corresponding isotope distribution (shown in Figure S1), these are attributed to the formation of $C_5F_3^-$, $FSO_2^-$, and $CF_3^-$, respectively.

## High intensity DEA fragments from pentafluorophenyl triflate

Figure 2 shows the ion yield curves for the high intensity fragments formed in DEA to pentafluorophenyl triflate in the energy range from around 0–12 eV; $CF_3SO_3^-$, m/z 149 (A), $CF_3SO_2^-$, m/z 133 (B), and $C_6F_5O^-$, m/z 183 (C). The respective structures, optimized at the B3LYP/def2-TZVP level of theory are shown as insets. Table 1 shows the threshold energies ($E_{Th}$) for all fragments observed in DEA to pentafluorophenyl, calculated at the B3LYP/def2-TZVP level of theory as the difference of the total energy of the neutral parent and the fragments formed, computed at the same level of theory. Also shown is the vertical electron affinity of pentafluorophenyl triflate, calculated at the same level of theory. Total energies, zero-point energies, thermal corrections, and entropy contributions of the neutral parent and all relevant fragments are given in Table S1. The threshold values for m/z 117 ($C_5F_3^-$) and m/z 83 ($FSO_2^-$), shown in Table 1, are for the lowest energy rearrangement reactions found in the current calculations (see Table S2), while all other threshold values are calculated for the respective single bond rupture processes.

As DEA is a resonant process the threshold values represent the lowest energy at which the respective fragment may be formed if there are no reaction barriers. The actual appearance in the ion yield is, however, determined by the resonance transition probability and decay dynamics.[10] Thus, only exothermic processes may proceed through the close to 0 eV resonances, where the attachment cross section is the highest and the autodetachment rate the lowest, hence, where dissociation is an effective relaxation channel. Correspondingly, the minimal prerequisites for a PAG to be activated by DEA in the EUVL process are that the respective dissociation process is exothermic and that the MO structure supports resonant electron capture at very low energies.

As may be seen from Table 1, the formation of all three high-intensity fragments observed in DEA to pentafluorophenyl triflate is found to be exothermic at the B3LYP/def2-TZVP level of theory, and the main contribution for all three is through a narrow peak with a maximum at about 0.1 eV incident electron energy. From these, the $CF_3SO_3^-$ (m/z 149) ion yield, is markedly asymmetric toward higher energy but with no further structured contributions in this low energy range. We assign this asymmetry of the 0.1 eV $CF_3SO_3^-$ (m/z 149) peak to two distinct resonant contributions, the first being associated with single electron occupation of the lowest unoccupied molecular orbital (LUMO), and the second with single electron occupation of the LUMO+1 and/or LUMO+2 of the neutral. This is signified in Figure 3A, which shows a combined fit to the low energy $CF_3SO_3^-$ (m/z 149) ion yield, composed of a normal Gaussian, representing the low energy contribution (LUMO) and a skewed Gaussian representing the higher energy contribution (LUMO+1/LUMO+2). For the complementary ions $C_6F_5O^-$ (m/z 183, Figure 3B) and $CF_3SO_2^-$ (m/z 133, Figure S2), the third low energy contribution peaking at about 1.25 eV is also fitted with a skewed Gaussian. As an initial guess for the peak positions, the experimental values of 0.1 and 1.25 eV were taken for the lowest and highest energy contribution, and for the LUMO+1/LUMO+2 contribution the average of their relative orbital energies with respect to the LUMO (0.45 eV) was taken as the initial guess, assuming a 100 meV shift toward lower energy with respect to the calculated relative orbital energies. This fitting approach is taken, as we expect the autodetachment rate to play a significant role at higher energies, making these contributions more significant in their low energy range[10] (see the method section).

When comparing the relative peak cross sections for the formation of these three fragments, it is clear that dissociation through single electron occupation of the LUMO predominantly leads to the formation of $CF_3SO_3^-$ (m/z 149) and $CF_3SO_2^-$ (m/z 133). In fact, the formation of $CF_3SO_3^-$ (m/z 149) is the most significant channel, appearing with more than an order of

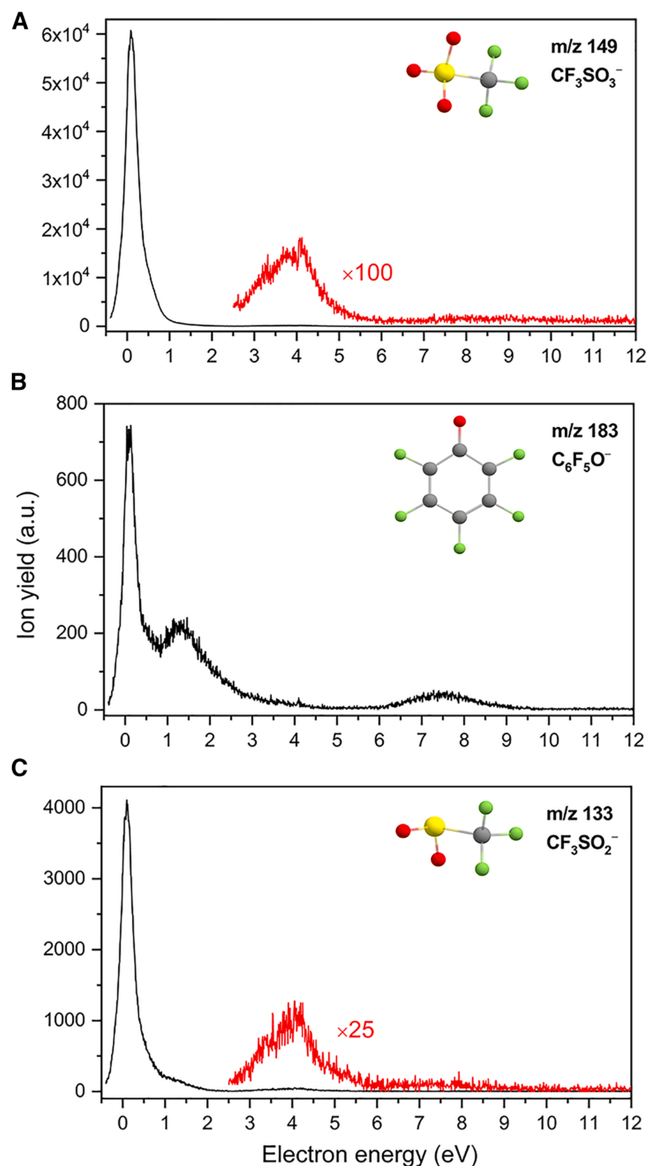


**Figure 2. Ion yield curves for the high intensity DEA fragments from pentafluorophenyl triflate**

(A) $C_6F_5O^-$ (m/z 183), (B) $CF_3SO_2^-$ (m/z 149), and (C) $CF_3SO_2^-$ (m/z 133) (also see Figure S2).

magnitude higher intensity than $CF_3SO_2^-$ (m/z 133), which in turn appears with an order of magnitude higher intensity than the corresponding aromatic rest $C_6F_5O^-$ (m/z 183). The formation of $C_6F_5^-$ (m/z 167) is endothermic with $E_{th}$ = 0.36 eV at the B3LYP/def2-TZVP level of theory and thus not accessible at this low energy and is only observed with marginal intensities through a higher lying resonance peaking at about 7.8 eV (see Figure S3).

Figure 4 shows contour plots of the lowest lying MOs of the neutral *and anionic* pentafluorophenyl triflate presented with a contour value of 0.05 au. The LUMO, LUMO+1, and LUMO+2 of the ground state neutral pentafluorophenyl triflate are shown

**Table 1. Threshold energies ($E_{Th}$) for all fragments observed in DEA to pentafluorophenyl triflate**

| m/z | Product(s) | $E_{Th}$ (eV) |
|---|---|---|
| 316 | $M^-$: $[C_6F_5O–S(O)_2CF_3]^-$ Vertical attachment energy | −0.30 |
| 183 | $[C_6F_5O]^-$ + $CF_3SO_2$ | −1.61 |
| 167 | $[C_6F_5]^-$ + $CF_3SO_3$ | 0.36 |
| 149 | $[CF_3SO_3]^-$ + $C_6F_5$ | −1.53 |
| 133 | $[CF_3SO_2]^-$ + $C_6F_5O$ | −1.93 |
| 117 | $[C_5F_3]^-$ + $CF_2O$ + $CF_3SO_2$ | 1.85 |
| 83 | $[FSO_2]^-$ + $C_6F_5$ + $CF_2O$ | −1.78 |
| 69 | $[CF_3]^-$ + $C_6F_5OSO_2$ | 0.45 |

in the first line, and the corresponding highest occupied molecular orbital (HOMO) (singly occupied molecular orbital [SOMO]), LUMO, and LUMO+1 of the ground state pentafluorophenyl triflate anion are shown in lines two and three. The latter are shown for the anion in the frozen geometry of the neutral ground state (second line) and for the anionic ground state after geometry relaxation (third line). This is shown as we find the relaxed ground state geometry of the anion to be unstable at the B3LYP/def2-TZVP level of theory, dissociating by rupture of the S–OC bond of the sulfonic ester. The LUMO of the neutral parent is found to be of π* character and largely located on the benzene ring, i.e., corresponding to the $b_1$ (π*) of $C_{2v}$-substituted benzene as assigned by Jordan et al.[60] Similarly, the LUMO+1 of the neutral is also of π* character, corresponding to the $a_2$ (π*) of $C_{2v}$-substituted benzenes, while the LUMO+2 is the lowest lying unoccupied σ* orbital of the neutral. Hence, the π*/σ* inversion, observed due to the strong inductive effect of the fluorines in perfluorinated benzenes,[61,62] is not apparent here. We also found this to be the case in a recent study on DEA to pentafluorobenzoic acid,[63] and similarly, we attribute this here to strong coupling of the sulfonic substituent with the π-system of the aromatic ring, i.e., a mesomeric effect mainly stabilizing the $b_1$ π* LUMO but also the $a_2$ π* LUMO+1 with respect to the σ* LUMO+2 of the neutral. In the parent anion, the influence of the stabilizing mesomeric effect is apparently reduced. In the frozen geometry the singly occupied HOMO of the anion (LUMO of the neutral) is still the $b_1$ π*; however, the LUMO (LUMO+1 of the neutral) is found to be of a σ* character while the LUMO+1 of the anion (LUMO+2 of the neutral) is the $a_2$ π* orbital in the $C_{2v}$ notation. We however note that according to our B3LYP/def2-TZVP calculations the energy difference between these orbitals, the LUMO+1 and LUMO+2 of the neutral, is only about 50 meV.

In good agreement with our experimental data the HOMO (SOMO) of the anionic ground state of pentafluorophenyl triflate is antibonding along the S–OC coordinate, and in fact the geometry relaxation of the ground state anion leads to rupture of this bond. We thus anticipate that the dominating, close to 0 eV contributions in the $CF_3SO_3^-$, $CF_3SO_2^-$, and $C_6F_5O^-$ ion yields, are provided through initial transition to the ground state anion, i.e., a single electron occupation of the LUMO of the neutral ground state pentafluorophenyl triflate. We further anticipate that the apparent discrepancy of the computed relaxation leading to

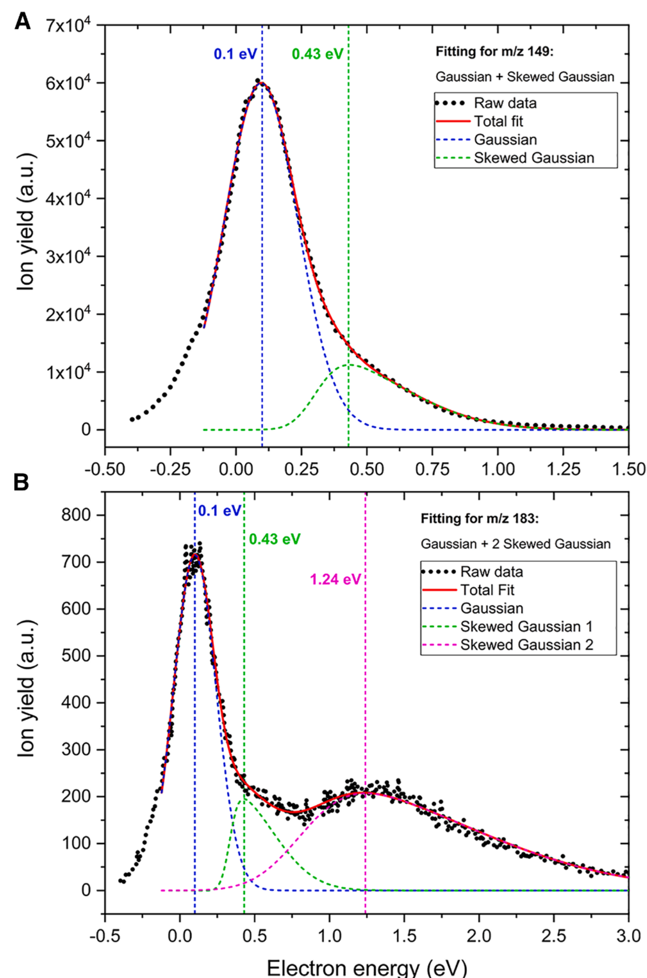


**Figure 3. Combined fit to the highest low-energy DEA yields from pentafluorophenyl triflate**

(A) $CF_3SO_3^-$ (m/z 149) and (B) $C_6F_5O^-$ (m/z 183). The normal Gaussian peaking at 0.1 eV and the skewed Gaussians peaking at 0.43 eV about 1.2 eV represent the contributions attributed to occupation of the LUMO, LUMO+1/LUMO+2 and LUMO+3 of the neutral, respectively (also see Figure S3).

$CF_3SO_2^-$ (m/z 133) while the $CF_3SO_3^-$ (m/z 149) is the highest intensity fragment observed from the ground state, is due to effective vibrational coupling of the π* HOMO of the anion with the SO–C antibonding σ* LUMO. I.e., such dynamic coupling is not provided in the 0 K geometrical relaxation of the anion while it is provided through vibrational states occupied at the 298 K of the experiments.[10,64] The higher energy contribution providing the asymmetry of the $CF_3SO_3^-$ 0.1 eV peak, on the other hand, is attributed to direct dissociation from the SO–C antibonding σ* LUMO of the anion, though initial occupation of the ($a_2$) π* LUMO+1 of the neutral (LUMO+2 of the anion) may also contribute.

## Low intensity DEA fragments from pentafluorophenyl triflate

In addition to the high intensity contributions close to 0 eV, a significant contribution is observed to the complementary $CF_3SO_2^-$ (m/z 133) and $C_6F_5O^-$ (m/z 183) yields, with peaks at around 1.25 eV. This contribution is also significant in the lower intensity ion yields for the formation of $CF_3^-$ (m/z 69) and $FSO_2^-$ (m/z 83) but is absent in the $C_5F_3^-$ (m/z 117) ion yield. This may be seen in Figure 5, which shows the ion yield curves for the lower intensity fragments from DEA to pentafluorophenyl triflate in the energy range of 0–12 eV, i.e., $CF_3^-$, $FSO_2^-$, and $C_6F_5O^-$, along with their lowest energy structures optimized at the B3LYP/def2-TZVP level of theory. As the formation of all fragments through this resonance are associated with bond ruptures within the triflate substituent, this resonance is most likely associated with single electron occupation of a molecular orbital strongly located on the triflate group. Correspondingly, we tentatively assign these contributions to single electron occupation of the LUMO+3 of the neutral (LUMO+2 of the anion), where this is the case for the relaxed anion (see Figure S4). This also matches relatively well with the 1.7 eV LUMO/LUMO+3 energy difference calculated at the B3LYP/def2-TZVP level of theory.

For the formation of $CF_3^-$ through single bond rupture, we find a threshold of 0.45 eV. This is also apparent in the $CF_3^-$ ion yield, where this contribution is shifted to higher energy as compared to $CF_3SO_2^-$ (m/z 133) and $C_6F_5O^-$ (m/z 183). The $FSO_2^-$ ion yield through this resonance, on the other hand, peaks at about 1.3 eV. The formation of this fragment requires significant rearrangement, and assuming the formation of the neutral difluoro formaldehyde ($F_2CO$) in this reaction, as has been shown for other complex rearrangement reactions in DEA,[65] we find the threshold to be – 1.78 eV (see Table 1). This is also apparent in the higher $FSO_2^-$ ion yield through this resonance as compared to $CF_3^-$, reflecting the inverse energy dependence of the autodetachment rate.

Finally, there are fairly broad low intensity contributions in the ion yields from about 3 to 5 eV and 6–9 eV. At the B3LYP/def2-TZVP level of theory we find the HOMO-LUMO gap to be about 6 eV (see Figure 4), and we thus anticipate that the former are due to shape resonance(s) in this energy range while the latter is likely to be from higher energy core-excited resonance(s). Interestingly $C_5F_3^-$ is formed through the lower lying resonance(s) with a high relative intensity. We attribute that to a rearrangement reaction leading again to the formation of neutral $F_2CO$, but now through fragmentation of the aromatic ring and the formation of the lowest energy configuration of the anion. Complete account of all thresholds calculated and the respective structures, including values for different isomers and alternative reaction paths to other fragments, are given in Table S2.

## DISCUSSION

Here we have conducted a combined experimental and theoretical study on DEA to pentafluorophenyl triflate; $CF_3SO_2$–O–$C_6F_5$, a compound belonging to a group of neutral esters under consideration as PAGs, hypothesized to enhance the sensitivity of CAR formulations for their use in EUVL. These neutral PAGs are specifically of interest to enable higher PAG loads without phase separation, as both the quantum yield and photon count is low in EUVL as compared to the conventional DUVL scanners.[48,49] In pentafluorophenyl triflate the trifluoromethanesulfonate (triflate) group constitutes the acid precursor, and homolytic

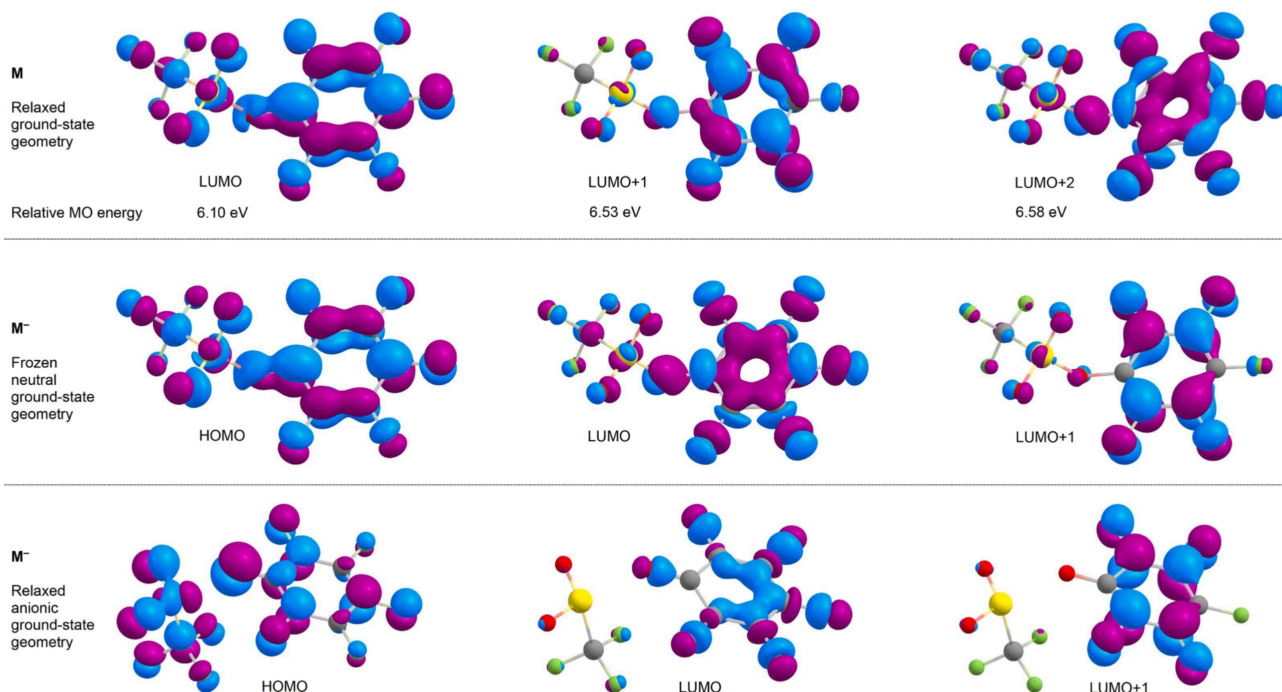


**Figure 4. Contour plots of the lowest lying MOs of the neutral and anionic pentafluorophenyl triflate (also see Figure S4)**
First line: LUMO, LUMO+1, and LUMO+2 of the geometry relaxed ground state neutral. Second line: the singly occupied HOMO, the LUMO, and LUMO+1 of the ground state anion in the frozen geometry of neutral ground state. Third line: the singly occupied HOMO, the LUMO, and LUMO+1 of the ground state anion after geometry relaxation.

rupture of the ester bond to the phenyl group leads to the formation of the triflate radical. This radical then extracts a hydrogen from other components of the resist formulation, to form the strong protic trifluoromethanesulfonic acid.[49] In DEA to pentafluorophenyl triflate we find the main channels to be the formation of $CF_3SO_3^-$, $CF_3SO_2^-$, and $C_6F_5O^-$ at very low electron incident energies, while lower intensity fragments are formed through shape and core excited resonances at higher energies. The prerequisite for pentafluorophenyl triflate to act as acid generator in EUVL CARs, however, is the electron-induced generation of the $CF_3SO_3$ radical as a precursor for the respective acid formation. Contrary to this, the current study shows clearly that DEA to pentafluorophenyl triflate predominantly forms $CF_3SO_3^-$, the closed-shell, neutral complimentary base to the triflic acid, and no signs of the formation of the triflic radical intermediate, leading to the targeted formation of the very strong triflic acid are observed.

Moreover, from the observed ion yields and computed MO structures and thermochemistry, we show that this may be expected to be general for DEA to asymmetric neutral ester PAGs. In DEA, the bond rupture is generally homolytic, however, the products in a single DEA bond rupture process are a radical and a closed-shell anionic fragment. Furtheremore, charge retention in such DEA processes is generally on the more electronegative fragment. This in turn constitutes the acid precursor when considering neutral ester PAGs, i.e., the triflate group in the current case. Hence, DEA to neutral ester PAGs, leads to the formation of the closed shell anion of the acid precursor, which constitutes the pH neutral, complementary base of the strong acid whose generation is targeted. DEA thus blocks the pre-acid of such neutral ester PAGs from further hydrogen abstraction and thus from the formation of the respective "photoacid". This applies in general and is very apparent in the current study where the dominating fragment is the thermochemically stable closed-shell $CF_3SO_3^-$, i.e., the triflic acid anion, instead of the corresponding radical needed for the acid generation.[49] Furthermore, no potential neutral radicals that could act as acid precursors were found to be formed through DEA in the current study. Thus, DEA of this group of PAGs quinces the acid formation, rather than promoting it as is the intention in CARs for EUVL. In EUVL, this is bound to lower the photon-to-acid conversion yield of these PAGs significantly, and viable paths to include the highly efficient DEA process in the acid generation, providing significant improvement of the performance of these PAGs, are needed.

In this context a potential path to tailor an effective neutral acid generator that is triggered through DEA, would be to combine two strongly electronegative pre-acids in such a way that a single bond rupture through DEA would lead to formation of both the closed shell anion and the neutral radical of the respective pre-acid(s). Potential candidates for such compounds would be neutral derivatives of the peroxydisulphuric acid such as the peroxy dimer of the triflate, the trifluoromethane-sulfonic peroxyanhydride ($CF_3S(O)_2$–O–O–$S(O)_2CF_3$). To our knowledge, this compound is, however, not commercially available, but considering that the ester bond rupture through DEA in the current experiments is significant on both the S–O and the O–C side of the

CellPress
OPEN ACCESS

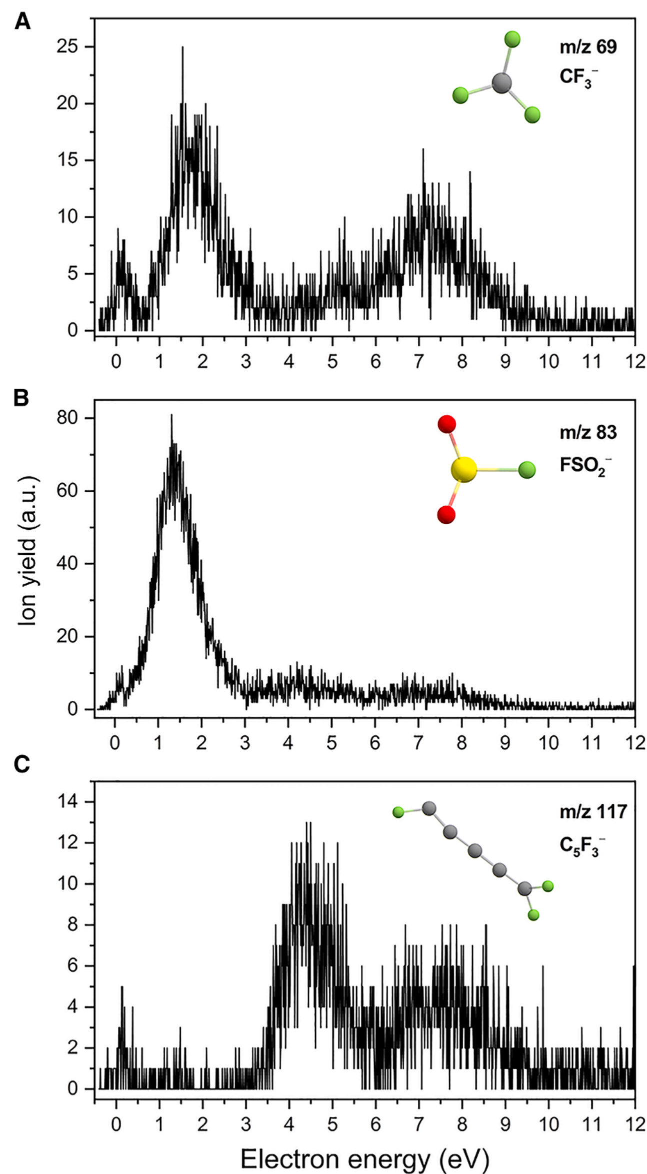


**Figure 5. Ion yield curves for the low intensity DEA fragments from pentafluorophenyl triflate**

(A) $CF_3^-$ (m/z 69), (B) $FSO_2^-$ (m/z 83), and (C) $C_5F_3^-$ (m/z 117) (also see Figure S1).

ester, with $CF_3S(O)_2^-$ being a significant fragment, the commercially available trifluoromethanesulfonic anhydride ($CF_3S(O)_2$–O–$S(O)_2CF_3$) is a candidate worthwhile looking at. At the B3LYP/def2-TZVP level of theory we find the formation of the $CF_3SO_3$ radical to be exothermic for both these compounds through single bond rupture, leading to $CF_3SO_3^-$ and $CF_3SO_2^-$ as the respective counter ions. Furthermore, similar to pentafluorophenyl triflate, geometry relaxation of the parent anions of both these compounds, at the same level of theory, leads to rupture of the respective bonds relevant to the $CF_3SO_3$ radical formation, i.e., the O–O peroxy bond of the sulfonic peroxyanhydride and one of the O–S bonds of the sulfonic anhydride, respectively. Both these compounds may thus be considered good candidates for the formation of the $CF_3SO_3$ radical through DEA (see Figures S5 and S6; Tables S3 and S4).

It should, however, be kept in mind that the secondary electron energy distribution in EUV exposure of resist materials is dynamic. Hence for every electron active in the very low energy DEA range, at least one ionization process has taken place as well as several other inelastic scattering processes, including electronic excitations. Thus, DI and ND are also bound to play a role, providing a complex scenario of the combination of the branching ratios and cross sections for the individual processes.

## Limitations of the study

The current study focuses on the fundamental, chemical processes of EUVL resist components in direct relation to the expected performance of the respective resist formulations. Though the induced chemistry is fundamental to the performance of the resist material, and a prerequisite for its applicability, systematic evaluation of properties and performance parameters such as solvent compatibility, coating quality, and patterning performance in terms of resolution, LER, and sensitivity is necessary to transform this chemistry to resist formulations applicable in industrial EUVL processes.

## RESOURCE AVAILABILITY

### Lead contact

Requests for further information and resources should be directed to and will be fulfilled by the lead contact Oddur Ingólfsson (odduring@hi.is).

### Materials availability

This study did not generate new unique reagents.

### Data and code availability

- Raw data have been deposited at Zenodo as dataset: https://doi.org/10.5281/zenodo.16761593. Additionally, ORCA output files are available as dataset: https://doi.org/10.5281/zenodo.16761422.
- This paper does not report original code.
- Any additional information required to reanalyze the data reported in this paper is available from the lead contact upon request.

## ACKNOWLEDGMENTS

P.G., M.M., and F.F.d.S. acknowledges the Portuguese National Funding Agency FCT through the research grant number UID/FIS/00068/2020 (https://doi.org/10.54499/UIDP/00068/2020) (CEFITEC). M.M. acknowledges FCT through the research grant 2023.14518.PEX. O.I. acknowledges The Icelandic Center for Research for the research grant number 185346-05, and R.T. the University of Iceland PhD fund. The authors thank Dr. Maicol Cipriani for constructive discussions and for fitting data.

## AUTHOR CONTRIBUTIONS

M.M. and R.T.: investigation, validation, verification, formal analysis, visualization, and review & editing. P.G.: investigation. F.H.: conceptualization, resources, methodology, and review & editing. F.F.d.S.: conceptualization, project administration, supervision, resources, methodology, and review & editing. O.I.: conceptualization, project administration, supervision, resources, methodology, writing original draft, and review & rditing.

## DECLARATION OF INTERESTS

The authors declare no competing interests.

## STAR★METHODS

Detailed methods are provided in the online version of this paper and include the following:

- KEY RESOURCES TABLE
- METHOD DETAILS
  - Experimental
  - Quantum chemical calculations
- QUANTIFICATION AND STATISTICAL ANALYSIS

## SUPPLEMENTAL INFORMATION

Supplemental information can be found online at https://doi.org/10.1016/j.isci.2025.114020.

Received: June 10, 2025
Revised: July 29, 2025
Accepted: November 7, 2025
Published: November 11, 2025

## REFERENCES

1. Kazazis, D., Santaclara, J.G., van Schoot, J., Mochi, I., and Ekinci, Y. (2024). Extreme ultraviolet lithography. Nat. Rev. Methods Primers *4*, 84. https://doi.org/10.1038/s43586-024-00361-z.
2. Levinson, H.J., and Brunner, T.A. (2018). Current challenges and opportunities for EUV lithography. In Proc. SPIE 10809, International Conference on Extreme Ultraviolet Lithography, pp. 1080903. https://doi.org/10.1117/12.2502791.
3. Okazaki, S. (1991). Resolution limits of optical lithography. J. Vac. Sci. Technol. B Microelectron. Nanom. Struct. Process. Meas. Phenom. *9*, 2829–2833. https://doi.org/10.1116/1.585650.
4. Bhardwaj, A., Dash, D., Anant, A., Bhanushali, V.M., Kushwah, A., Mishra, I., Shubham, and Kumar Pandey, C. (2025). Comprehensive Analysis on Complementary FET. IEEE Access *13*, 82554–82572. https://doi.org/10.1109/ACCESS.2025.3568134.
5. Kostko, O., McAfee, T.R., Ma, J., Blackwell, J.M., and Naulleau, P. (2024). Experimental characterization of model extreme ultraviolet resist materials. J. Micro/Nanopatterning. Mater. Metrol. *23*, 14602. https://doi.org/10.1117/1.JMM.23.1.014602.
6. Torok, J., Re, R.D., Herbol, H., Das, S., Bocharova, I., Paolucci, A., Ocola, L.E., Ventrice, C., Jr., Lifshin, E., Denbeaux, G., and Brainard, R.L. (2013). Secondary Electrons in EUV Lithography. J. Photopol. Sci. Technol. *26*, 625–634. https://doi.org/10.2494/photopolymer.26.625.
7. Kozawa, T., and Tagawa, S. (2010). Radiation Chemistry in Chemically Amplified Resists. Jpn. J. Appl. Phys. *49*, 030001. https://doi.org/10.1143/JJAP.49.030001.
8. Dapor, M., Masters, R.C., Ross, I., Lidzey, D.G., Pearson, A., Abril, I., Garcia-Molina, R., Sharp, J., Unčovský, M., Vystavel, T., et al. (2018). Secondary electron spectra of semi-crystalline polymers – A novel polymer characterisation tool? J. Electron Spectros. Relat. Phenomena *222*, 95–105. https://doi.org/10.1016/j.elspec.2017.08.001.
9. Fallica, R., Nannarone, S., Mahne, N., Malvezzi, A.M., Berti, A., and Simone, D.D. (2021). Evolution of Secondary Electrons Emission During EUV Exposure in Photoresists. J. Photopol. Sci. Technol. *34*, 99–103. https://doi.org/10.2494/photopolymer.34.99.
10. Ingólfsson, O. (2019). Low-Energy Electrons Fundamentals and Applications, First edition (Jenny Stanford Publishing).
11. Pollentier, I., Vesters, Y., Jiang, J., Vanelderen, P., and De Simone, D. (2017). Unraveling the role of secondary electrons upon their interaction with photoresist during EUV exposure. In Proc. SPIE 10450, International Conference on Extreme Ultraviolet Lithography 2017, 104500H (16 October 2017). https://doi.org/10.1117/12.2281449.
12. Thete, A., Geelen, D., Wuister, S., van der Molen, S.J., and Tromp, R.M. (2015). Low-energy electron (0-100eV) interaction with resists using LEEM. Proc. SPIE *9422*, 94220A. https://doi.org/10.1117/12.2085369.
13. Grzeskowiak, S., Kaminsky, J., Gibbons, S., Murphy, M., Chandonait, J., Brainard, R.L., and Denbeaux, G. (2018). Polymer effects on PAG acid yield in EUV resists. Proc. SPIE 10586, Advances in Patterning Materials and Processes XXXV, 105860D (21 March 2018). https://doi.org/10.1117/12.2297692.
14. Grzeskowiak, S., Kaminsky, J., Gibbons, S., Narasimhan, A., Brainard, R.L., and Denbeaux, G. (2018). Electron trapping: a mechanism for acid production in extreme ultraviolet photoresists. J. Micro/Nanolith. MEMS MOEMS *17*, 33501. https://doi.org/10.1117/1.JMM.17.3.033501.
15. Rathore, A., Pollentier, I., Cipriani, M., Singh, H., De Simone, D., Ingólfsson, O., and De Gendt, S. (2021). Extreme Ultraviolet-Printability and Mechanistic Studies of Engineered Hydrogen Silsesquioxane Photoresist Systems. ACS Appl. Polym. Mater. *3*, 1964–1972. https://doi.org/10.1021/acsapm.1c00018.
16. Bespalov, I., Zhang, Y., Haitjema, J., Tromp, R.M., Van Der Molen, S.J., Brouwer, A.M., Jobst, J., and Castellanos, S. (2020). Key Role of Very Low Energy Electrons in Tin-Based Molecular Resists for Extreme Ultraviolet Nanolithography. ACS Appl. Mater. Interfaces *12*, 9881–9889. https://doi.org/10.1021/acsami.9b19004.
17. Itani, T., and Kozawa, T. (2013). Resist Materials and Processes for Extreme Ultraviolet Lithography. Jpn. J. Appl. Phys. *52*, 010002. https://doi.org/10.7567/JJAP.52.010002.
18. Fujii, S., Okamoto, K., Yamamoto, H., Kozawa, T., and Itani, T. (2017). Sensitivity enhancement of chemically amplified EUV resists by adding acid-generating promoters. Jpn. J. Appl. Phys. *56*, 06GD01. https://doi.org/10.7567/JJAP.56.06GD01.
19. Buitrago, E., Nagahara, S., Yildirim, O., Nakagawa, H., Tagawa, S., Meeuwissen, M., Nagai, T., Naruoka, T., Verspaget, C., Hoefnagels, R., et al. (2016). Sensitivity enhancement of chemically amplified resists and performance study using extreme ultraviolet interference lithography. J. Micro/Nanolith. MEMS MOEMS *15*, 033502. https://doi.org/10.1117/1.JMM.15.3.033502.
20. Jiang, J., Giordano, G., Fallica, R., DeSimone, D., and Vandenberghe, G. (2019). Sensitizer for EUV Chemically Amplified Resist: Metal versus Halogen. J. Photopol. Sci. Technol. *32*, 21–25. https://doi.org/10.2494/photopolymer.32.21.
21. Yamamoto, H., Vesters, Y., Jiang, J., Simone, D.D., Vandenberghe, G., and Kozawa, T. (2018). Role of Metal Sensitizers for Sensitivity Improvement in EUV Chemically Amplified Resist. J. Photopol. Sci. Technol. *31*, 747–751. https://doi.org/10.2494/photopolymer.31.747.
22. Belmonte, G.K., Cendron, S.W., Guruprasad Reddy, P., Moura, C.A.S., Ghulam Moinuddin, M., Peter, J., Sharma, S.K., Albara Lando, G., Puiatti, M., Gonsalves, K.E., and Weibel, D.E. (2020). Mechanistic insights of Sn-based non-chemically-amplified resists under EUV irradiation. Appl. Surf. Sci. *533*, 146553. https://doi.org/10.1016/j.apsusc.2020.146553.
23. Wang, Z., Chen, J., Yu, T., Zeng, Y., Guo, X., Wang, S., Allenet, T., Vockenhuber, M., Ekinci, Y., Yang, G., and Li, Y. (2023). Sulfonium-Functionalized Polystyrene-Based Nonchemically Amplified Resists Enabling Sub-13 nm Nanolithography. ACS Appl. Mater. Interfaces *15*, 2289–2300. https://doi.org/10.1021/acsami.2c19940.
24. Moura, C.A.d.S., Belmonte, G.K., Reddy, P.G., Gonslaves, K.E., and Weibel, D.E. (2018). EUV photofragmentation study of hybrid nonchemically amplified resists containing antimony as an absorption enhancer. RSC Adv. *8*, 10930–10938. https://doi.org/10.1039/C7RA12934C.
25. Reddy, P.G., Mamidi, N., Kumar, P., Sharma, S.K., Ghosh, S., Gonsalves, K.E., and Pradeep, C.P. (2016). Design, development, EUVL applications

CellPress
OPEN ACCESS

and nano mechanical properties of a new HfO2 based hybrid non-chemically amplified resist. RSC Adv. *6*, 67143–67149. https://doi.org/10.1039/C6RA10575K.

26. Wu, L., Baljozovic, M., Portale, G., Kazazis, D., Vockenhuber, M., Jung, T., Ekinci, Y., and Castellanos, S. (2019). Mechanistic insights in Zr- and Hf-based molecular hybrid EUV photoresists. J. Micro/Nanolith. MEMS MOEMS *18*, 1. https://doi.org/10.1117/1.JMM.18.1.013504.
27. Hasan, M.W., Deeb, L., Kumaniaev, S., Wei, C., and Wang, K. (2024). Recent Advances in Metal-Oxide-Based Photoresists for EUV Lithography. Micromachines *15*, 1122. https://doi.org/10.3390/mi15091122.
28. Haitjema, J., Zhang, Y., Vockenhuber, M., Kazazis, D., Ekinci, Y., and Brouwer, A.M. (2017). Extreme ultraviolet patterning of tin-oxo cages. J. Micro/Nanolith. MEMS MOEMS *16*, 1. https://doi.org/10.1117/1.JMM.16.3.033510.
29. Thakur, N., Bliem, R., Mochi, I., Vockenhuber, M., Ekinci, Y., and Castellanos, S. (2020). Mixed-ligand zinc-oxoclusters: efficient chemistry for high resolution nanolithography. J. Mater. Chem. C *8*, 14499–14506. https://doi.org/10.1039/D0TC03597A.
30. Thakur, N., Tseng, L.-T., Ekinci, Y., and Castellanos, S. (2019). Stability studies on a sensitive EUV photoresist based on zinc metal oxoclusters. J. Micro/Nanolithography, MEMS, MOEMS *18*, 43504. https://doi.org/10.1117/1.JMM.18.4.043504.
31. Si, Y., Zhao, Y., Shi, G., Zhou, D., Luo, F., Chen, P., Fan, J., and Peng, X. (2023). A novel stable zinc–oxo cluster for advanced lithography patterning. J. Mater. Chem. A *11*, 4801–4807. https://doi.org/10.1039/D3TA00115F.
32. Kosma, V., Kasahara, K., Xu, H., Odent, J., Ober, C.K., and Giannelis, E.P. (2017). Elucidating the patterning mechanism of zirconium-based hybrid photoresists. J. Micro/Nanolith. MEMS MOEMS *16*, 1. https://doi.org/10.1117/1.JMM.16.4.041007.
33. Cardineau, B., Del Re, R., Marnell, M., Al-Mashat, H., Vockenhuber, M., Ekinci, Y., Sarma, C., Freedman, D.A., and Brainard, R.L. (2014). Photolithographic properties of tin-oxo clusters using extreme ultraviolet light (13.5nm). Microelectron. Eng. *127*, 44–50. https://doi.org/10.1016/j.mee.2014.04.024.
34. Saifullah, M.S.M., Rajak, A.K., Hofhuis, K.A., Tiwale, N., Mahfoud, Z., Testino, A., Karadan, P., Vockenhuber, M., Kazazis, D., Valiyaveettil, S., and Ekinci, Y. (2024). Approaching Angstrom Scale Resolution in Lithography Using Low. ACS Nano *18*, 24076–24094. https://doi.org/10.1021/acsnano.4c03939.
35. Liu, F.-F., Shi, G.-Y., Zhen, N., Zhou, Z.-H., Guo, T.-L., Qiao, Y., Zhao, J., Liu, J.-C., Luo, F., and Zhang, L. (2025). Single Rare-Earth Ion Doped Tin-Oxo Nanocluster Photoresists for High-Resolution Extreme Ultraviolet Lithography. Nano Lett. *25*, 2067–2073. https://doi.org/10.1021/acs.nanolett.4c06140.
36. Qiao, Y., Shi, G., Zhang, O., Li, Y., Vockenhuber, M., Ekinci, Y., Luo, F., and Zhang, L. (2024). Heterometallic Ti-Zr oxo nanocluster photoresists for advanced lithography. Sci. China Mater. *67*, 3132–3141. https://doi.org/10.1007/s40843-024-3013-9.
37. Xu, H., Sakai, K., Kasahara, K., Kosma, V., Yang, K., Herbol, H.C., Odent, J., Clancy, P., Giannelis, E.P., and Ober, C.K. (2018). Metal–Organic Framework-Inspired Metal-Containing Clusters for High-Resolution Patterning. Chem. Mater. *30*, 4124–4133.
38. Käfer, F., Wang, C., Huang, Y., Segalman, R., and Ober, C.K. (2023). Polypeptoids: Exploring the Power of Sequence Control in a Photoresist for Extreme-Ultraviolet Lithography. Adv. Mater. Technol. *8*, 2301104. https://doi.org/10.1002/admt.202301104.
39. Takei, S., Oshima, A., Oyama, T.G., Ito, K., Sugahara, K., Kashiwakura, M., Kozawa, T., Tagawa, S., and Hanabata, M. (2014). Application of natural linear polysaccharide to green resist polymers for electron beam and extreme-ultraviolet lithography. Jpn. J. Appl. Phys. *53*, 116505. https://doi.org/10.7567/JJAP.53.116505.
40. Frommhold, A., Yang, D., McClelland, A., Xue, X., Ekinci, Y., Palmer, R.E., and Robinson, A.P.G. (2013). Performance of negative tone chemically amplified fullerene resists in extreme ultraviolet lithography. J. Micro/Nanolith. MEMS MOEMS *12*, 033010. https://doi.org/10.1117/1.JMM.12.3.033010.
41. Ober, C.K., Kafer, F., and Deng, J. (2022). Review of essential use of fluorochemicals in lithographic patterning and semiconductor processing. J. Micro/Nanopatterning, Mater. Metrol. *21*, 10901. https://doi.org/10.1117/1.JMM.21.1.010901.
42. Wu, L., Bespalov, I., Witte, K., Lugier, O., Haitjema, J., Vockenhuber, M., Ekinci, Y., Watts, B., Brouwer, A.M., and Castellanos, S. (2020). Unravelling the effect of fluorinated ligands in hybrid EUV photoresists by X-ray spectroscopy. J. Mater. Chem. C *8*, 14757–14765. https://doi.org/10.1039/D0TC03216F.
43. Kruger, S., Revuru, S., Higgins, C., Gibbons, S., Freedman, D.A., Yueh, W., Younkin, T.R., and Brainard, R.L. (2009). Fluorinated Acid Amplifiers for EUV Lithography. J. Am. Chem. Soc. *131*, 9862–9863. https://doi.org/10.1021/ja901448d.
44. Wang, M., Yueh, W., and Gonsalves, K.E. (2008). Fluorine-contained photoacid generators (PAGs) and corresponding polymer resists. J. Fluor. Chem. *129*, 607–612. https://doi.org/10.1016/j.jfluchem.2008.04.014.
45. Okamoto, K., Nomura, N., Fujiyoshi, R., Umegaki, K., Yamamoto, H., Kobayashi, K., and Kozawa, T. (2017). Dynamics of Radical Ions of Hydroxyhexafluoroisopropyl-Substituted Benzenes. J. Phys. Chem. A *121*, 9458–9465. https://doi.org/10.1021/acs.jpca.7b09842.
46. Kumar, P., Reddy, P.G., Sharma, S.K., Ghosh, S., Pradeep, C.P., and Gonsalves, K.E. (2018). Enhanced mechanical properties of the high-resolution EUVL patterns of hybrid photoresists containing hexafluoroantimonate. Microelectron. Eng. *194*, 100–108. https://doi.org/10.1016/j.mee.2018.03.014.
47. Torti, E., Protti, S., Bollanti, S., Flora, F., Torre, A., Brusatin, G., Gerardino, A., Businaro, L., Fagnoni, M., Mezi, L., and Della Giustina, G. (2018). Aryl Sulfonates as Initiators for Extreme Ultraviolet Lithography: Applications in Epoxy-Based Hybrid Materials. ChemPhotoChem *2*, 425–432.
48. Manouras, T., and Argitis, P. (2020). High Sensitivity Resists for EUV Lithography: A Review of Material Design Strategies and Performance Results. Nanomater *10*, 1593. https://doi.org/10.3390/nano10081593.
49. Martin, C.J., Rapenne, G., Nakashima, T., and Kawai, T. (2018). Recent progress in development of photoacid generators. J. Photochem. Photobiol. C Photochem. Rev. *34*, 41–51. https://doi.org/10.1016/j.jphotochemrev.2018.01.003.
50. Nishimae, Y., Yamato, H., Asakura, T., and Ohwa, M. (2008). Non-ionic photoacid generators for chemically amplified resists: chromophore effect on resist performance. Proc. SPIE *6923*, 69233Q. https://doi.org/10.1117/12.770883.
51. Sulc, R., Blackwell, J.M., Younkin, T.R., Putna, E.S., Esswein, K., DiPasquale, A.G., Callahan, R., Tsubaki, H., and Tsuchihashi, T. (2009). Aryl sulfonates as neutral photoacid generators (PAGs) for EUV lithography. Proc. SPIE *7273*, 72733R. https://doi.org/10.1117/12.814279.
52. Xu, W., Li, T., Li, G., Wu, Y., and Miyashita, T. (2011). Novel polymeric nonionic photoacid generators and corresponding polymer Langmuir–Blodgett (LB) films for photopatterning. J. Photochem. Photobiol. Chem. *219*, 50–57. https://doi.org/10.1016/j.jphotochem.2011.01.015.
53. Sundararajan, N., Keimel, C.F., Bhargava, N., Ober, C.K., Opitz, J., Allen, R.D., Barclay, G., and Xu, G. (1999). Diffusion and Distribution Studies of Photoacid Generators: Ion Beam Analysis in Lithography. J. Photopol. Sci. Technol. *12*, 457–467. https://doi.org/10.2494/photopolymer.12.457.
54. Fedynyshyn, T.H., Astolfi, D.K., Cabral, A., and Roberts, J. (2007). PAG segregation during exposure affecting innate material roughness. Proc. SPIE *6519*, 65190X. https://doi.org/10.1117/12.713892.

55. Covert, K.L., and Russell, D.J. (1993). Distribution of onium salt photoinitiators in a two-phase epoxy system. J. Appl. Polym. Sci. *49*, 657–671. https://doi.org/10.1002/app.1993.070490411.

56. Peng, Y., Chen, P., Chen, H., Si, Y., and Peng, X. (2024). Absorption-coefficient calculation of short-wavelength photoresist materials: From EUV to BEUV and water window X-ray. Smart Mol. *2024*, e20240043. https://doi.org/10.1002/smo.20240043.

57. Ptasińska, S., Gschliesser, D., Bartl, P., Janik, I., Scheier, P., and Denifl, S. (2011). Dissociative electron attachment to triflates. J. Chem. Phys. *135*, 214309. https://doi.org/10.1063/1.3664784.

58. Herd, C.R., Smith, D., and Adams, N.G. (1989). A study of dissociative electron attachment to CF3SO3CH3 and CF3SO3C2H5 triflate esters using the FALP apparatus. Int. J. Mass Spectrom. Ion Process. *91*, 177–182. https://doi.org/10.1016/0168-1176(89)83007-1.

59. Laffert, V., Sajjadian, F.S., Richter, R., van Setten, M.J., and Holzmeier, F. (2024). Dissociative photoionization of phenyl triflate, a photoacid generator for photolithography, at 92 eV. J. Chem. Phys. *160*, 134303. https://doi.org/10.1063/5.0203648.

60. Jordan, K.D., Michejda, J.A., and Burrow, P.D. (1976). Electron transmission studies of the negative ion states of substituted benzenes in the gas phase. J. Am. Chem. Soc. *98*, 7189–7191. https://doi.org/10.1021/ja00439a014.

61. Brundle, C.R., Robin, M.B., and Kuebler, N.A. (1972). Perfluoro effect in photoelectron spectroscopy. II. Aromatic molecules. J. Am. Chem. Soc. *94*, 1466–1475. https://doi.org/10.1021/ja00760a008.

62. Hitchcock, A.P., Fischer, P., Gedanken, A., and Robin, M.B. (1987). Antibonding .sigma.* valence MOs in the inner-shell and outer-shell spectra of the fluorobenzenes. J. Phys. Chem. *91*, 531–540. https://doi.org/10.1021/j100287a009.

63. Cipriani, M., and Ingólfsson, O. (2023). Potential of HF and CO2 loss through dissociative electron attachment to increase radiosensitizers reactivity; case study on pentafluorobenzoic acid. Radiat. Phys. Chem. *202*, 1–6. https://doi.org/10.1016/j.radphyschem.2022.110544.

64. Nag, P., Tarana, M., and Fedor, J. (2021). Effects of $\pi^{*} - \sigma^{*}$ coupling on dissociative-electron-attachment angular distributions in vinyl, allyl, and benzyl chloride and in chlorobenzene. Phys. Rev. A *103*, 032830. https://doi.org/10.1103/PhysRevA.103.032830.

65. Ómarsson, B., and Ingólfsson, O. (2013). Stabilization, fragmentation and rearrangement reactions in low-energy electron interaction with tetrafluoro-para-benzoquinone; a combined theoretical and experimental study. Phys. Chem. Chem. Phys. *15*, 16758–16767. https://doi.org/10.1039/b000000x.

66. Pereira-Da-Silva, J., Rodrigues, R., Ramos, J., Brígido, C., Botnari, A., Silvestre, M., Ameixa, J., Mendes, M., Zappa, F., Mullock, S.J., et al. (2021). Electron Driven Reactions in Tetrafluoroethane: Positive and Negative Ion Formation. J. Am. Soc. Mass Spectrom. *32*, 1459–1468. https://doi.org/10.1021/jasms.1c00057.

67. Neese, F. (2012). The ORCA program system, program for quantom chemical calculation. Wiley Interdiscip. Rev. Comput. Mol. Sci. *2*, 73–78. https://doi.org/10.1063/5.0004608.

68. Becke, A.D. (1993). Density-functional thermochemistry. III. The role of exact exchange. J. Chem. Phys. *98*, 5648–5652. https://doi.org/10.1063/1.464913.

69. Stephens, P.J., Devlin, F.J., Chabalowski, C.F., and Frisch, M.J. (1994). Ab Initio calculation of vibrational absorption and circular dichroism spectra using density functional force fields. J. Phys. Chem. *98*, 11623–11627. https://doi.org/10.1021/j100096a001.

70. Tirado-rives, J., and Jorgensen, W.L. (2008). Performance of B3LYP Density Functional Methods for a Large Set of Organic Molecules. J. Chem. Theory Comput. *4*, 297–306.

71. Torres, E., and Dilabio, G.A. (2012). A (Nearly) Universally Applicable Method for Modeling Noncovalent Interactions Using B3LYP. J. Phys. Chem. Lett. *3*, 1738–1744.

72. Weigend, F., and Ahlrichs, R. (2005). Balanced basis sets of split valence, triple zeta valence and quadruple zeta valence quality for H to Rn: Design and assessment of accuracy. Phys. Chem. Chem. Phys. *7*, 3297–3305. https://doi.org/10.1039/b508541a.

CellPress
OPEN ACCESS

# STAR★METHODS

## KEY RESOURCES TABLE

| REAGENT or RESOURCE | SOURCE | IDENTIFIER |
|---|---|---|
| Chemicals, peptides, and recombinant proteins | | |
| Pentafluorophenyl triflate; | Sigma-Aldrich | CAS Number: 60129-85-3 |
| Carbon tetrachloride anhydrous (For energy calibration) | Sigma-Aldrich | CAS Number: 56-23-5 |
| Deposited data | | |
| Experimental raw data | This paper | https://doi.org/10.5281/zenodo.16761593 |
| Output files, Quantum chemical calculational, Orca | This paper | https://doi.org/10.5281/zenodo.16761422 |
| Software and algorithms | | |
| ORCA software package (version 5 and 6.1) | On line | https://orcaforum.kofo.mpg.de/app.php/portal |
| ChemCraft - graphical software for visualization of quantum chemistry computations. Version 1.8. | On line | https://www.chemcraftprog.com |
| Python™ Version 3.13 | On line | https://www.python.org |

## METHOD DETAILS

### Experimental

The current measurements were performed with a crossed electron-molecular beam apparatus consisting of a trochoidal electron monochromator (TEM) coupled with ToF-MS in an orthogonal geometry, described elsewhere.[66] Briefly, a quasi-monoenergetic electron beam is generated from the TEM, with a resolution of about ~200 meV. The electron current is monitored by an amperemeter connected to a faraday plate and is found to be ~40 nA at ~0eV. The anions formed are extracted by a weak electrical field (~1V/cm) into an ion guide and further mass analysed with a ToF-MS and detected with a multi-channel plate detector. The energy scale of the ion yield curves was calibrated with $CCl_4$ by setting the lowest energy $Cl^-$ formation as 0 eV. The data acquisition and data analysis were performed with home-made LabVIEW and python programmes, respectively. The sample was purchased from Sigma Aldrich, with 97% purity. The liquid sample was purified by passing through 4 freeze-pump-thaw cycles. The molecular vapor was introduced in the chamber and the experiments were carried out at $3.5\times10^{-4}$ Pa.

### Quantum chemical calculations

All quantum chemical calculations were conducted utilizing the ORCA software package (version 5 and 6.1)[67] and ChemCraft - graphical software vas used for visualization of MO contours. The geometries of molecules were optimized, and corresponding single-point energy calculations were performed using density functional theory (DFT) employing the Becke three-parameter Lee–Yang–Parr hybrid functional (B3LYP)[68–71] together with the def2-TZVP valence triple-zeta polarization basis set.[72] Closed-shell molecular systems were treated with the restricted Kohn-Sham (RKS) formalism, whereas open-shell systems were described using the unrestricted Kohn-Sham (UKS) formalism. Harmonic vibrational frequency calculations were executed at the same theoretical level to verify that optimized structures represented a true minimum on the potential energy surface (characterized by the absence of imaginary frequencies). These vibrational analyses were also used to obtain zero-point vibrational energies (ZPVEs) and thermal corrections for both neutral parent molecules and ionic fragments at 298 K.

Threshold energies associated with potential fragmentation pathways corresponding to experimentally observed mass-to-charge (m/z) ratios were computed by subtracting the sum of the calculated single-point energies of product fragments from the energy of the neutral precursor molecule. All reported threshold energies include the ZPVEs and thermal energy corrections determined at the DFT level of theory.

## QUANTIFICATION AND STATISTICAL ANALYSIS

Fittings to the $CF_3SO_2^-$, $CF_3SO_3^-$ and $C_6F_5O^-$ ion yields were performed with Python, using the SciPy library with an initial guess of the mean for the lowest energy contribution of 0.1 eV and for the highest of 1.25 eV both from the experimental values. For the

LUMO+1/LUMO+2 contribution the initial guess was 0.45 eV, allowing for about 100 meV shift to lower energy from the average of the calculated LUMO-LUMO+1 and LUMO-LUMO+2 values, thus accounting for the inverse energy dependence of the autodetachment lifetime. For $CF_3SO_2^-$ (m/z 133) and $CF_3SO_3^-$ (m/z 149) a free fit with these initial guesses gave a RS value of 0.9972 and 0.9999, respectively, with peak values of 0.1, 0.47 and 1.23 eV, and 0.1 and 0.43 eV, respectively. For $C_6F_5O^-$ (m/z 183) the mean of the first gaussian was fixed at 0.1 and for the second skewed gaussian the skewness factor was fixed at 3. This gave peak values of 0.43 and 1.24 eV for the two higher energy Gaussian fits with an RS value of 0.9910.